# We are IntechOpen, the world's leading publisher of Open Access books Built by scientists, for scientists

**4,800**
Open access books available

**122,000**
International authors and editors

**135M**
Downloads

Our authors are among the

**154**
Countries delivered to

**TOP 1%**
most cited scientists

**12.2%**
Contributors from top 500 universities


WEB OF SCIENCE™

Selection of our books indexed in the Book Citation Index in Web of Science™ Core Collection (BKCI)

## Interested in publishing with us?
## Contact book.department@intechopen.com

Numbers displayed above are based on latest data collected.
For more information visit www.intechopen.com

Chapter 17

# OFDM and SC-FDMA over Fiber Using Directly Modulated VCSELs

Henrique M. Salgado, Rúben E. Neto,
Luís M. Pessoa and Pedro J. Batista

Additional information is available at the end of the chapter

http://dx.doi.org/10.5772/61118

**Abstract**

Radio-over-fiber technology, used in the transport of radio signals over optical fiber by means of an optical carrier between a remote site and a central node of a cellular network, is an attractive solution for backhauling of a large number of remote antennas, enabling the shifting of the hardware complexity from base stations to a central station.

Integration of both optical and wireless broadband infrastructures into the same backhaul network leads to significant simplification and cost reduction of base stations permitting equipment sharing and dynamic allocation of resources, which in turn leads to simplified system operation and maintenance.

Wireless systems on the other hand are evolving rapidly and new standards are appearing, such as the Long-Term Evolution aiming at satisfying the required need for increasing bandwidth. Radio-over-fiber systems are known to be susceptible to noise and non-linear distortion in particular to the large peak-to-average power ratio of orthogonal frequency division multiplexing signals employed in these standards. In this work we compare, experimentally and through simulation, the performance of orthogonal frequency division multiplexing and single carrier frequency division multiple access signals, in radio-over-fiber applications, using directly modulated VCSELs.

**Keywords:** RoF, VCSEL, OFDM, SC-FDMA

## 1. Introduction

Radio-over-fiber (RoF) technology is used in transporting radio signals over optical fiber by means of an optical carrier between a remote site and a central node of a cellular network. RoF techniques are increasingly seen as a promising solution to facilitate the backhauling of a large number of remote antennas, enabling the shifting of the hardware complexity from base stations to the central station [1]. RoF allows for the combination of the advantages of optical systems such as their high bandwidth and low power consumption, with the advantages of wireless systems, namely the flexibility to use multiple standards such as Long-Term Evolution (LTE) or other upcoming standards.

The number of LTE users has been increasing due to advantages such as the ability to reach a peak throughput of 300 Mbps on the downlink and 75 Mbps on the uplink [2]. To achieve high radio spectral efficiency as well as enable efficient scheduling in time and frequency domains, a multicarrier approach for multiple access was chosen by the 3rd Generation Partnership Project. Orthogonal frequency division multiple access (OFDMA) and single carrier frequency division multiple access (SC-FDMA) were selected for the downlink and uplink, respectively, the latter also known as discrete Fourier transform–spread OFDMA.

## 2. Motivation

When OFDMA or SC-FDMA type of signals are transmitted through directly modulated vertical-cavity surface emitting lasers (VCSELs), they suffer from intermodulation distortion, due to the large number of electrical subcarrier combination in the laser cavity which degrades system performance in addition to relative intensity noise (RIN), clipping noise at the transmitter as well as shot noise and thermal noise at the receiver.

This phenomenon is well known in the literature [3], and is a result of the interaction between the electrons and photons in the active region, which is generally well described by the rate equations [4]. As a motivation for this problem, Figure 1 and Figure 2 show the spectrum of an OFDM electrical signal at the laser output (after conversion by means of a photodiode), for two values of the laser bias current, 3 and 6 mA, respectively. The original OFDM signal is centred at 1 GHz, and directly modulates the VCSEL. The high nonlinear distortion of the signal (with centre at 1 GHz) can be clearly seen, which is caused by intermodulation distortion. Third order intermodulation products (IMPs) of the type, $f_i + f_j - f_k$ or $2f_i - f_j$, where $f_{i,j,k}$, represents the frequency of the OFDM subcarriers, coincide with the transmission band of the signal and severely limit system performance. The number of intermodulation terms falling on channel $r$, $IM_{111}^{N}(r)$, $IM_{21}^{N}(r)$, of type $f_i + f_j - f_k$ and $2f_i - f_j$, respectively, where $N$ is the number of subcarriers, is given as follows [5]:

$$IM_{21}^{N} = \frac{1}{2}\left\{N - 2 - \frac{1}{2}\left[1 - \left(-1\right)^{N}\right]\left(-1\right)^{r}\right\} \tag{1}$$

http://dx.doi.org/10.5772/61118

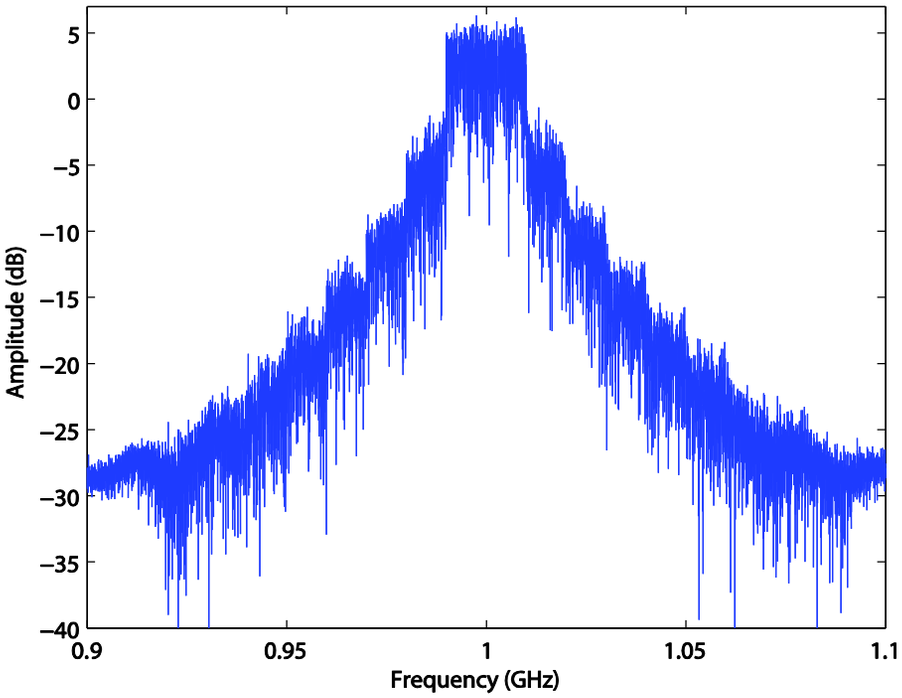


**Figure 1.** OFDM spectrum at the laser output for 3 mA bias current.

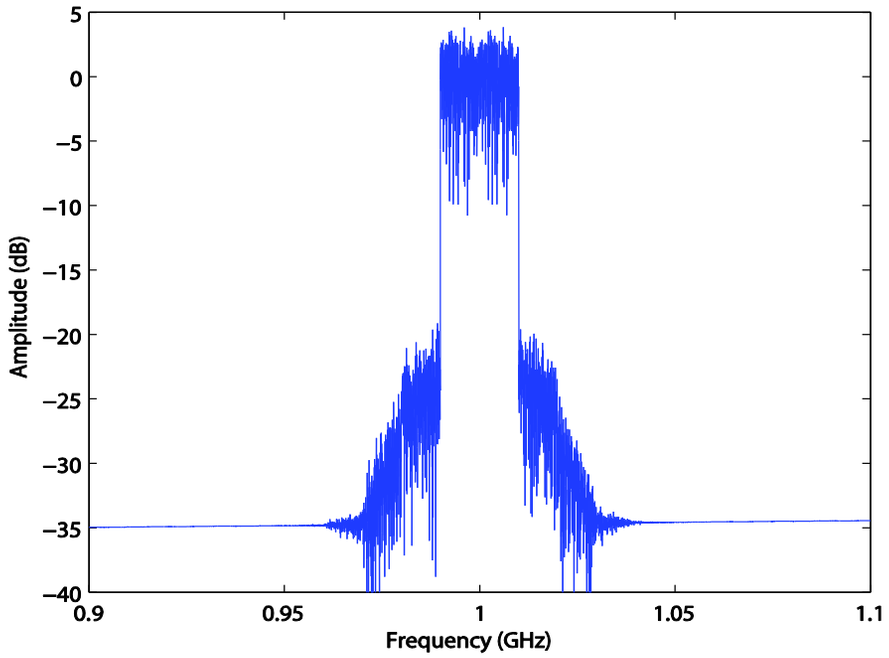


**Figure 2.** OFDM spectrum at the laser output for 6 mA bias current.

$$IM_{11\bar{1}}^{N} = \frac{r}{2}\left(N-r+1\right)+\frac{1}{4}\left[\left(N-3\right)^{2}-5\right]-\frac{1}{8}\left[1-\left(-1\right)^{N}\right]\left(-1\right)^{N+r} \tag{2}$$

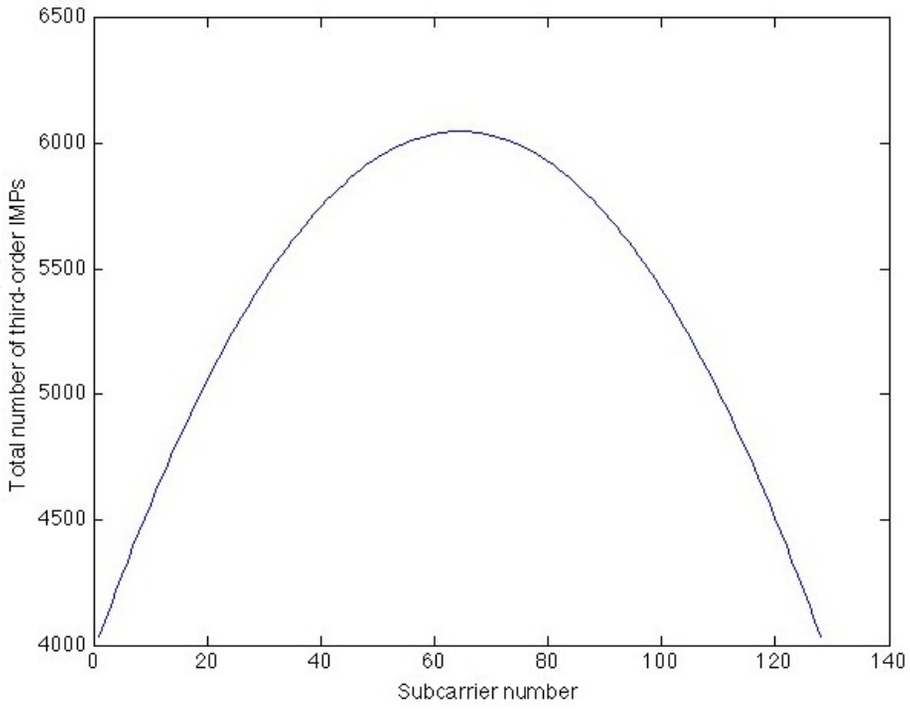


**Figure 3.** Total number of third-order intermodulation products as a function of subcarrier number for a 128 subcarriers signal.

Figure 3 shows the total number of third-order IMPs as a function of channel number, for 128 subcarriers. For a large number of subcarriers $IM_{111}^{N}$ and $IM_{21}^{N}$, approach the asymptotic value of $3N^2/8$ and $N/2$, respectively. On the other hand, the output spectrum is highly dependent on the operating point of the laser and on the allocation of the channels relative to the resonance frequency of the laser. On increasing the bias current to 6 mA, the resonance frequency, which previously was centred at 1 GHz, moves away to 2.5 GHz; therefore, the output signal presents a lower distortion as depicted in Figure 2. The interplay between the biasing of the laser, subcarriers frequency operation and noise, be it shot noise or RIN of the laser, is a complex one that needs to be modeled accurately for an adequate assessment of system performance. Hence, it is important to obtain a realistic model of the VCSEL device, including the electrical circuit associated with the parasitic elements and for that effect to extract the relevant parameters from experimental measurements.

## 3. Vertical-cavity surface-emitting laser

The VCSEL has emerged as an important class of semiconductor lasers in recent years. Its main characteristics, associated with the vertical-cavity geometry, are light emission perpendicular to the surface of the wafer and single longitudinal mode due to its short cavity length. The VCSEL is a microcavity laser consisting of a thin active region (< 1 μm) sandwiched between epitaxially grown distributed Bragg reflectors (DBRs). Since the first demonstration of the

VCSEL laser in Tokyo Institute of Technology in 1979 and after three decades of research, many potential applications have emerged. As a result several VCSEL manufacturers turned up in the market.

Due to their geometry, VCSELs offer a number of significant advantages over edge-emitting lasers listed below:

- Low threshold currents: the volume of the active region is relatively small, hence they possess low threshold currents and therefore consume less power than edge-emitting lasers.
- Circularly shaped beam: the symmetry in the wafer plane means the laser output is a narrow, low divergence circular beam, permitting high coupling efficiency to optical fibers with relaxed alignment tolerances.
- Single-mode operation: due to the microscopic cavity length, VCSELs inherently operate in a single-longitudinal mode which makes them suitable for high-bit-rate fiber optic communications.
- Low-cost-wafer fabrication: VCSELs allow for a high packing density in the form of two-dimensional arrays and cost-effective fabrication and testing at the wafer level.
- High modulation speed: experimental studies [3] indicate that the VCSELs have very fast intrinsic dynamic properties with relaxation oscillation frequencies as high as 71 GHz.

These advantages make the VCSEL device a suitable candidate for the applications targeted in ROF scenarios. However, the VCSEL as any semiconductor laser exhibits a nonlinear dynamic behavior that needs to be modeled accurately for the assessment of the impact of distortion on system performance. In the next section, the model of the VCSEL based on a set of rate equations for the carrier and photon density is presented. This model will be the basis for the investigation of the laser nonlinear distortion.

### 3.1. VCSEL modeling

The basic structure of the VCSEL is shown in Figure 4. The laser output is taken vertically through one of the mirrors, in contrast to conventional edge-emitting laser which emits light in the plane of the wafer surface. The conventional structure employs an active region consisting of multiple quantum wells between a n-type and a p-type DBR mirrors. Because of the short cavity length (≈ 1 μm) and thickness of the active region, the mirror reflectivities ($R$) of the DBRs must be greater than 99%. To achieve these high values of reflectivity, the DBR mirrors are made up of 20 to 40 alternating quarter-wavelength thick layers of high and low refractive indices made of semiconductors with different compositions, typically $Al_xGa_{(1-x)}As$.

The operation of a VCSEL can be understood by accounting for the rate of recombination of carriers in the active region and the rate of generation and loss of photons. For laser emission to occur, stimulated emission should be the dominant recombination mechanism. The threshold gain is defined as the gain required to sustain the optical field after travelling one round trip in the cavity. Assuming the optical gain is constant over the whole length of the laser, this leads to the condition

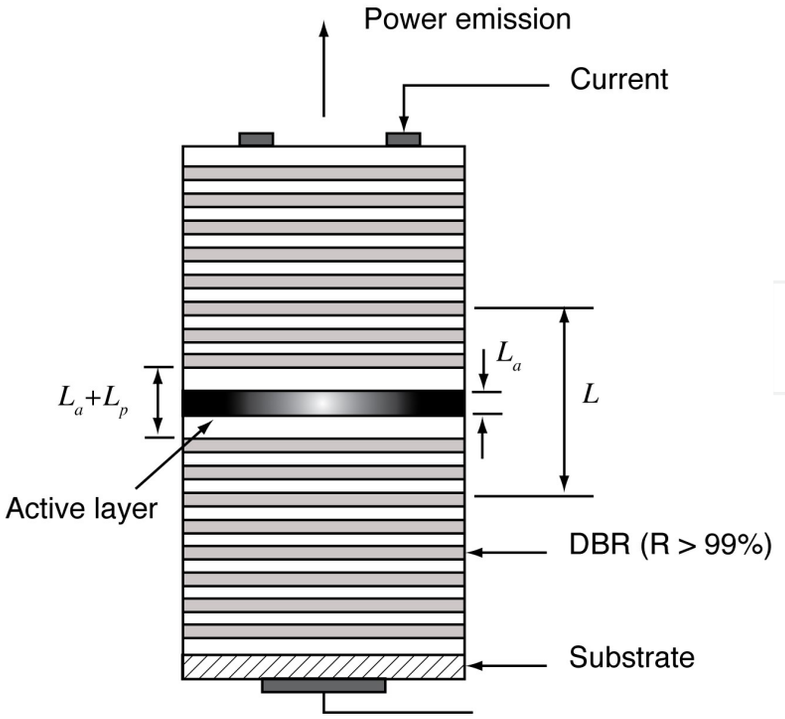


**Figure 4.** Schematic diagram of the laser structure, indicating active region thickness *La*, and effective cavity length *L*.

$$\Gamma g_{th} = \alpha_i + \frac{1}{L}\ln\left(\frac{1}{R}\right) \tag{3}$$

where $\Gamma$ is the optical confinement factor, $\alpha_i$ is the average internal loss and the second term is defined as the mirror loss $\alpha_m$. This equation shows that the gain per unit length must be sufficient to cancel out the optical losses and the losses due to light emission. Since the contribution of spontaneous emission in this simple analysis has not been considered, the actual gain will be slightly lower than the threshold gain. The description of laser operation is complete once the carrier density, $N$, is related to the injected current, $I$. This is accomplished through a rate equation that incorporates all the mechanisms by which the carriers are generated or lost inside the active region. The continuity equation which describes the rate of change of carriers in its general form is

$$\frac{dN}{dt} = \frac{\eta_i I}{qV} - \gamma_e(N)N - R_{st}P \tag{4}$$

The first term governs the rate at which the carriers are injected into the active layer due to external pumping; $q$ is the value of the electron charge, $\eta_i$ is the injection efficiency and $V$ is the volume of the active region. The second term takes into account the carrier loss owing to various recombination processes: spontaneous emission and non-radiation. The last term of

equation (4) is due to stimulated emission recombination that leads to coherent emission of light.

A suitable form for the carrier recombination rate $\gamma_e(N)$ and the corresponding carrier lifetime $\tau$, for lightly doped material is

$$\gamma_e\left(N\right)=\frac{1}{\tau}=A_{nr}+BN+CN^2 \tag{5}$$

where the terms with the coefficients $A_{nr}$, $B$, and $C$ represent defect, bimolecular recombination and Auger recombination, respectively.

A corresponding rate equation for the photon density can be obtained from the Maxwell's equations using a classical approach [4, 6]. By a simple bookkeeping of the supply, annihilation, and creation of carriers and photons inside the laser cavity, we get

$$\frac{dP}{dt}=P\left(\Gamma R_{st}-\frac{1}{\tau_p}\right)+\beta\Gamma R_{sp} \tag{6}$$

In which the photon lifetime is defined by

$$\tau_p^{-1}=v_g\left[\alpha_i+\frac{1}{L}\ln\left(\frac{1}{R}\right)\right] \tag{7}$$

Equation (6) states that the rate of increase in photon density is equal to the photon generation by stimulated emission $\Gamma R_{st}P$ less the loss rate of photons $-P/\tau_p$ (as characterized by the photon lifetime $\tau_p$), plus the rate of spontaneous emission into the photon mode $\beta R_{sp}$, where $\beta$ is the fraction of the total spontaneous emission coupled into the laser mode.

The net stimulated rate which tells us how many photons are generated per unit of time per existing photon, yields a generation rate of new photons $dP/dt$ according to the following equation

$$\frac{dP}{dt}=R_{st}P \tag{8}$$

The resulting stimulated gain coefficient relates to the stimulated emission coefficient, $R_{st}$, by

$$g=\frac{\text{power emitted per unit volume}}{\text{power crossing a unit area}}=\frac{\mathrm{R_{st}}}{v_g}=\frac{R_{st}\bar{\mu}}{c} \tag{9}$$

where $v_g$ is the group velocity, $c$ is the free-space velocity of light, and $\bar{\mu}$ is the group refractive index of the material taking dispersion into account: $[\bar{\mu}=(\mu+\nu d\mu/d\nu)]$. For a multiple quantum well laser, a logarithmic function of the carrier density fits the gain well over a wide range of $N$, (see [7]),

$$g(N)=g_c\log\left(\frac{N}{N_{0m}}\right) \tag{10}$$

where $N_{0m}$ is the carrier density for transparency (zero gain) and $g_c$ is the gain coefficient. The gain function may be linearized about the carrier density at transparency yielding [8],

$$g(N)\approx a(N-N_{0m})(1-\varepsilon P) \tag{11}$$

where $a$ is the differential gain, $\partial g/\partial N=g_c\cdot m/N_{0m}$and $m$ is a linearization parameter obtained so that $g_{log}(N)=g_{lin}(N)$ at threshold, that is for $N=N_{th}$. Gain compression is also accounted phenomenologically through the term $(1-\varepsilon P)$, $\varepsilon$ being the gain compression factor expressed in cubic meters.

Thus, we can rewrite the carrier and photon rate equations as

$$\frac{dN}{dt}=\frac{\eta_i I}{qV}-\frac{N}{\tau}-v_g a(N-N_{0m})(1-\varepsilon P)P \tag{12}$$

$$\frac{dP}{dt}=\Gamma v_g a(N-N_{0m})(1-\varepsilon P)P-\frac{1}{\tau_p}P+\beta\Gamma R_{sp} \tag{13}$$

The evolution of the signal transmitted over the optical fiber requires knowledge of the phase of the electric field. To account for dispersion effects, these equations may be complemented by an additional equation for the phase:

$$\frac{d\phi}{dt}=\frac{\alpha}{2}\left[\Gamma a v_g(N-N_{0m})-\frac{1}{\tau_p}\right] \tag{14}$$

where $\alpha$ is the linewidth enhancement factor. Equations (11-13) represent the basic relations for describing the dynamic characteristics of laser diodes, as long as the noise sources may be omitted.

The first-order transfer function of the intrinsic laser can be obtained by linearization of the previous equations and is given by the following equation

http://dx.doi.org/10.5772/61118

$$\frac{H_1(\omega)}{H_1(0)} = \frac{\gamma(1-\varepsilon p_0)p_0}{(j\omega)^2 + j\omega(\gamma\Gamma\beta j_{th}/p_0 + \gamma\varepsilon p_0) + \gamma(1-\varepsilon p_0)p_0} \tag{15}$$

$$\gamma = \frac{\tau}{\tau_p} \tag{16}$$

where for the ease of numerical calculation, the physical quantities have been normalized according to [9] and $p_0$, $n_0$ correspond to the steady-state values of the photon and carrier density within the active region, associated with the bias current, $j_{th}$

$$n_0 = g_0 \tau_p N_0 \tag{17}$$

$$p_0 = \frac{\beta n_0}{1/\Gamma + n_{0m} - n_0} \tag{18}$$

$$j_{th} \cong n_{th} = 1/\Gamma + n_{0m} \tag{19}$$

### 3.2. Package and chip parasitic elements

When dealing with high-frequency electronics, the frequency limits are usually established by the parasitic elements. It is then required to know whether the laser modulation characteristics are due to the laser alone or due to the parasitic elements. To this aim, one must treat the laser as an electrical element and establish an equivalent circuit that includes the parasitic elements. Characterization of an electrical network at high frequencies is usually done using the scattering parameters.

The elements of the laser-equivalent circuit are derived from the rate equations augmented by the heterojunction voltage-current and space-charge characteristics. The resulting equivalent circuit is a parallel RLC resonant circuit [9, 10]. The carrier density and quasi-Fermi levels are clamped above threshold which manifests in the equivalent circuit as an "ac" short and no voltage can develop. The magnitude of the impedance of the entire circuit $|Z(\omega)|$ is therefore essentially zero at all frequencies except near the relaxation oscillation resonance, where its value does not exceed ≈1 Ω. For deriving the relation between the total external current $I_s$ and the current through the active region $I_a$ and in comparison to the relatively large external elements, the intrinsic laser diode can be regarded as a short circuit at all frequencies. Under zero bias, the intrinsic laser can be modeled by the active layer space-charge capacitance [11].

Chip parasitic elements vary widely among different laser structures. In practice, they take the form of a resistance in series with the intrinsic device combined with a shunt capacitance. An

equivalent circuit model of the package and chip parasitic elements is shown in Figure 5; it includes a series inductor representing the wirebond, a shunting capacitor representing the contact capacitance, and a series resistor representing the contact resistance and the Bragg mirror stacks.

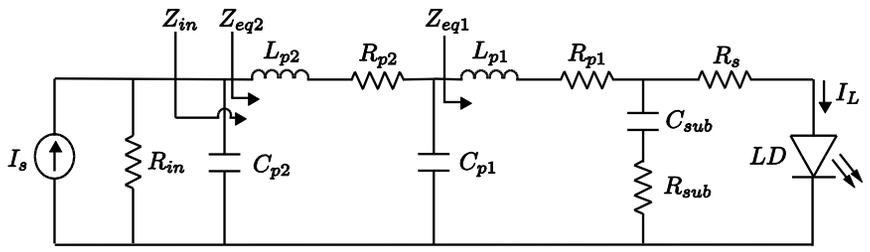


**Figure 5.** Equivalent circuit model for the laser parasitic elements.

We now define the following impedances:

$$Z_{p2} = R_{p2} + j\omega L_{p2} \tag{20}$$

$$Z_{p1} = R_{p1} + j\omega L_{p1} \tag{21}$$

$$Z_{sub} = R_{sub} + \frac{1}{j\omega C_{sub}} \tag{22}$$

The transfer function of the laser parasitic elements corresponding to ratio of the current flowing through the intrinsic laser, $I_L$ , and the source current, $I_S$, is given by:

$$Z_{in} = \frac{R_{in}}{1 + j\omega C_{p2} R_{in}} \tag{23}$$

$$Z_{eq1} = \frac{Z_{in} + Z_{p2}}{j\omega C_{p1}\left(Z_{in} + Z_{p2}\right)} \tag{24}$$

$$Z_{eq2} = \frac{Z_{eq1} + Z_{p1}}{Z_{sub} + Z_{eq1} + Z_{p1}} \tag{25}$$

$$\frac{I_L}{I_S} = \frac{Z_{eq1}}{Z_{eq1} + R_s} \frac{Z_{eq2}}{Z_{eq2} + Z_{p1}} \frac{Z_{in}}{Z_{in} + Z_{p2}} \tag{26}$$

The full laser transfer function is then the product of the intrinsic laser [equation (14)] and parasitic transfer functions (equation (26)).

### 3.3. Laser characterization

In modeling the VCSEL for simulation purposes, it is important to obtain a model as faithful as possible to the real device. This is achieved by extracting the laser parameters from experimental data. The $S_{21}$ and $S_{11}$ parameters are measured using a vectorial network analyzer (Lightwave Component Analyzer which characterizes devices in the electric and optical domains), a current source (Laser Diode Controller LDC-3700B), a bias-T (allows the continuous current injection in the laser), and a test fixture, as shown in Figure 6. The test fixture allows the connection between the laser and the SMA (Subminiature Version A) connector. The latter was designed in Advanced Design System considering Rogers 4000 series as a substrate. It should be noted that it is necessary to subtract the test fixture impact on the measurements using the de-embedding technique [12, 13].

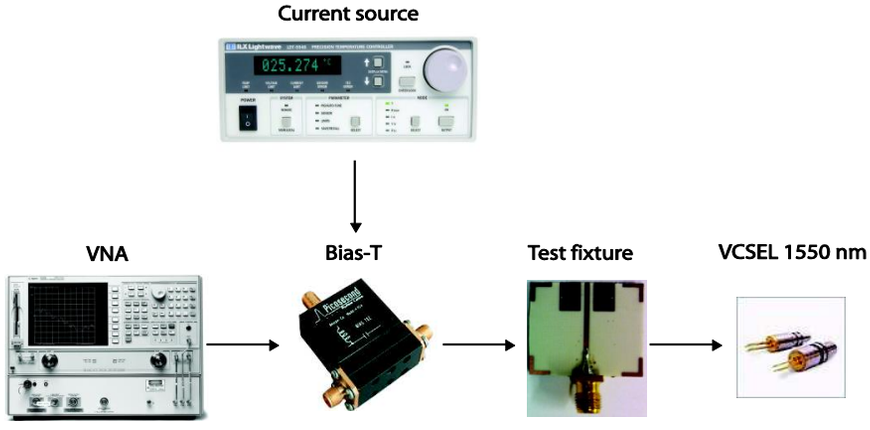


**Figure 6.** Setup for the measurement of the 1550 nm VCSEL.

### 3.4. Extraction of laser parasitic elements

It is possible to determine the input impedance $Z_{in}$ using the experimentally measured $S_{11}$ parameter:

$$Z_{in} = 50 \times \frac{1 + S_{11}}{1 - S_{11}} \tag{27}$$

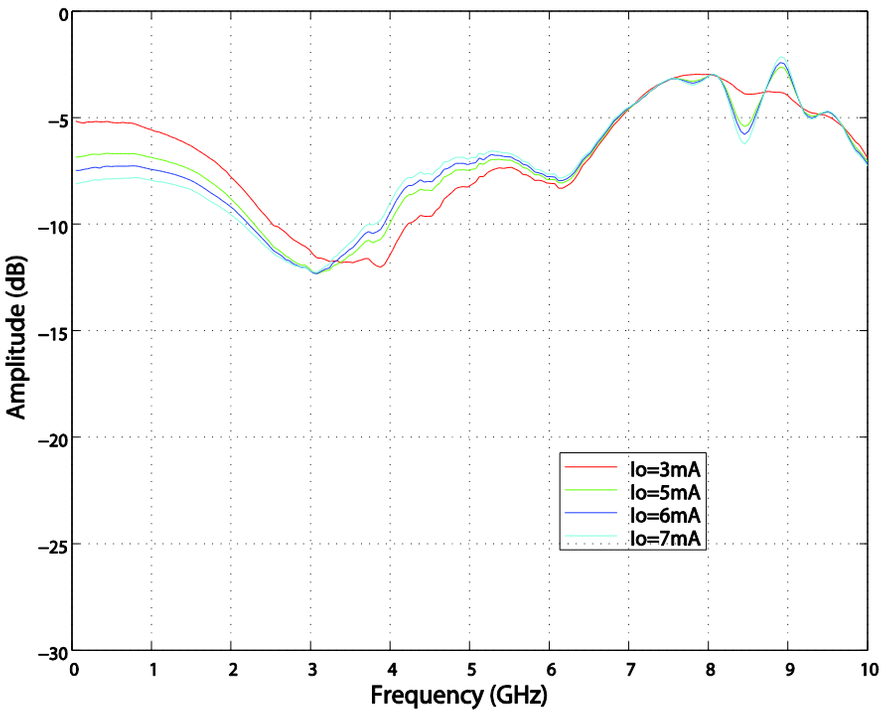


**Figure 7.** $S_{11}$ parameter for the 1550 nm VCSEL.

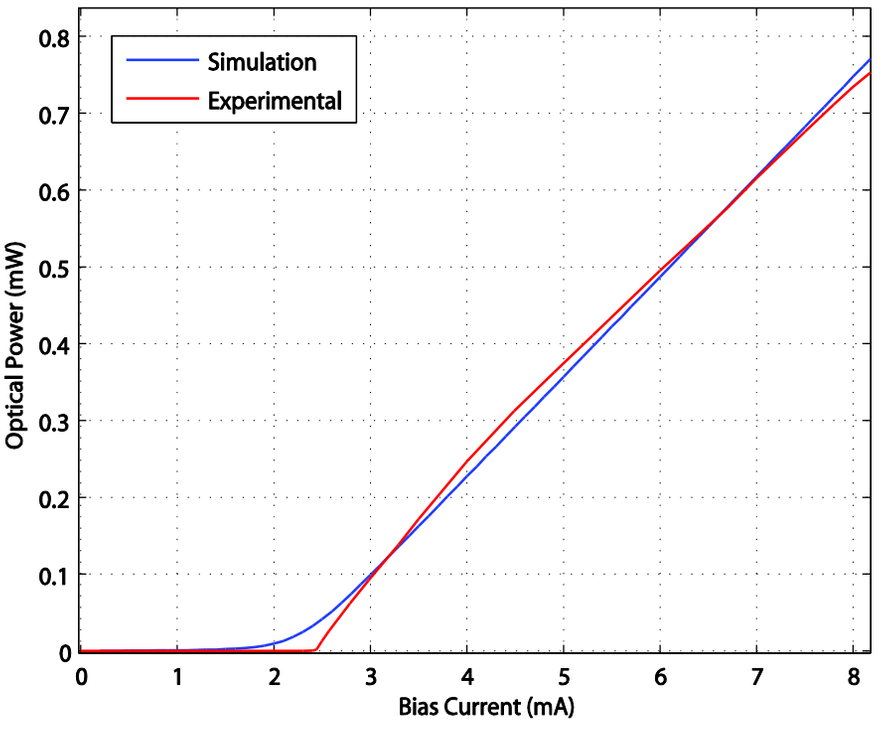


**Figure 8.** Characteristic curve for the 1550 nm VCSEL.

http://dx.doi.org/10.5772/61118

The measured $S_{11}$ parameter for the 1550 nm VCSEL for different bias currents above threshold is represented in Figure 7. The threshold current (2.14 mA) was obtained by inspection of the optical power versus current (*P-I*) characteristic curve shown in Figure 8.

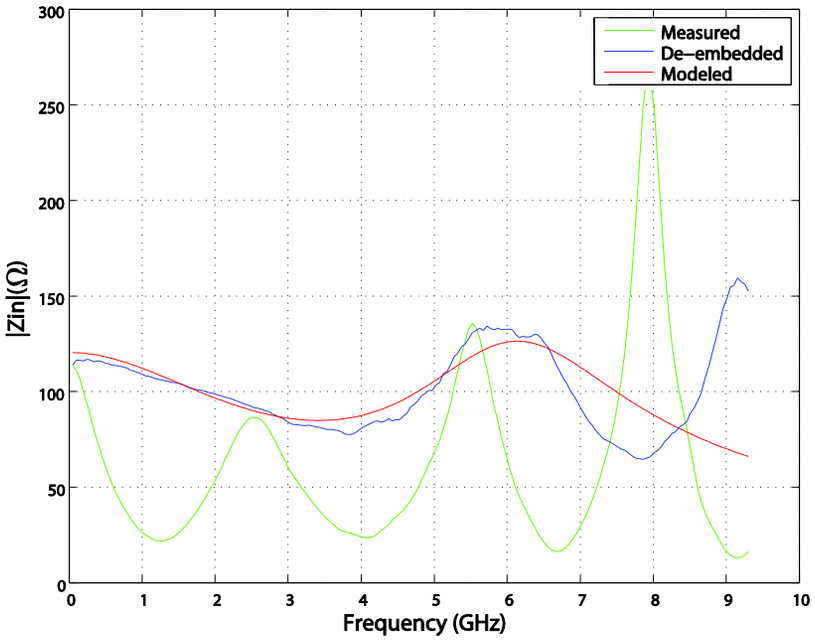


**Figure 9.** Magnitude of the 1550 nm VCSEL input impedance.

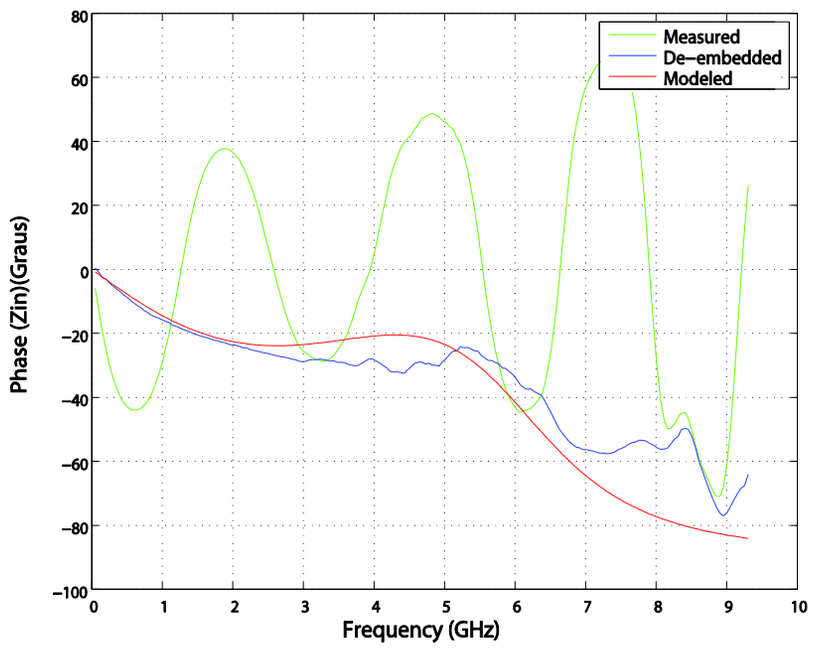


**Figure 10.** Phase of the 1550 nm VCSEL input impedance.

The laser parasitic elements are then obtained by means of an optimization process that fits the magnitude and phase of the input impedance of the equivalent circuit of the parasitics to the corresponding experimental result after the de-embedding procedure. From the results represented in Figure 9 and Figure 10, it is possible to verify the good approximation between the theoretical model (modeled) obtained using equation (23) and the experimental measurement (de-embedded), up to 7 GHz. Moreover, it is clear the importance of the de-embedding operation to obtain a good estimate of the laser parasitic elements.

The parasitic elements obtained before the optimization process are represented in Table 1:

| Element | Value | Element | Value |
|---|---|---|---|
| $R_{in}$ | 50 Ω | $L_{p1}$ | 0.68 nH |
| $C_{p2}$ | 0.3498 pF | $R_{p1}$ | 0.5 Ω |
| $L_{p2}$ | 2.828 nH | $C_{sub}$ | 0.04 pF |
| $R_{p2}$ | 52.387 Ω | $R_{sub}$ | 0 Ω |
| $C_{p1}$ | 0.6696 pF | $R_s$ | 113.02 Ω |

**Table 1.** Parasitic elements of the equivalent circuit

The frequency response of the circuit, as defined in equation (26), is shown in Figure 11, where the lowpass characteristic is observed.

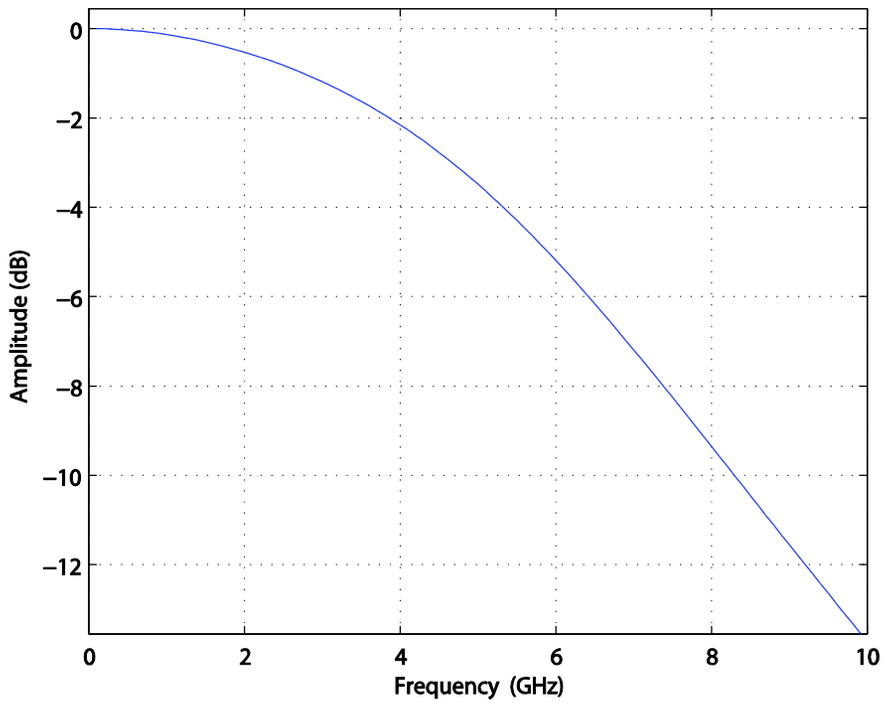


**Figure 11.** Normalized frequency response of the parasitic elements circuit.

http://dx.doi.org/10.5772/61118

### 3.5. Extraction of laser intrinsic parameters

The method employed for the extraction of the laser intrinsic parameters follows the frequency subtraction method described in reference [14]. To that purpose the laser transfer functions at different bias currents are obtained, using the $S_{21}$ parameter.

The experimental results, for different bias currents (above the threshold current), are represented as dashed lines in Figure 12. These results were used to extract the laser intrinsic parameters $[H_{ILD}(f)]$, by dividing each curve by the reference transfer function (measured for a bias current of 3 mA). The resulting function does not depend on the parasitic circuit $[H_{PC}(f)]$ or the test fixture $[H_{TC}(f)]$, as shown in equation (28) [15]:

$$\frac{H_{Global}\left(f,I_{Bias}\right)}{H_{Global}\left(f,I_{ref}\right)}=\frac{H_{ILD}\left(f,I_{Bias}\right)H_{PC}\left(f\right)H_{TC}\left(f\right)}{H_{ILD}\left(f,I_{ref}\right)H_{PC}\left(f\right)H_{TC}\left(f\right)}=\frac{H_{ILD}\left(f,I_{Bias}\right)}{H_{ILD}\left(f,I_{ref}\right)} \tag{28}$$

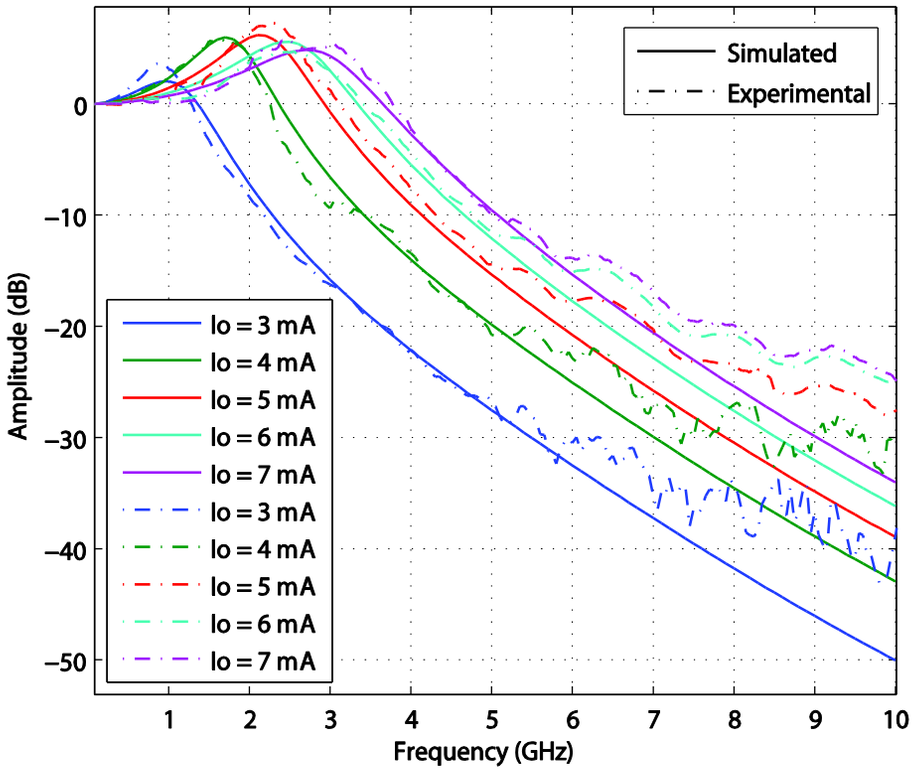


**Figure 12.** Frequency response of the 1550 nm VCSEL for different bias currents.

It is then possible to fit the corresponding theoretical response to the measured data through an optimization process of the laser parameters. That procedure was applied to the 1550 nm VCSEL, RC33xxx1-F from *RayCan*, using the Optimization Toolbox of MATLAB; the final result is shown in Table 2.

| Parameter | Value |
|---|---|
| $V$ , active region volume | $4.93\times10^{-18}$ $m^3$ |
| $g_{0,}$ gain slope constant | $2.50\times10^{12}$ $m^3s^{-1}$ |
| $N_{0m}$ , electron density at transparency | $2.71\times10^{24}$ $m^{-3}$ |
| $\beta$ , spontaneous emission factor | $6.5\times10^{-3}$ |
| $\Gamma$ , optical confinement factor | $3\times10^{-2}$ |
| $\tau_{s,}$ electron lifetime | 2.6 ns |
| $\tau_p$ , photon lifetime | 4.0 ps |
| $\varepsilon$ , gain compression factor | $5.0\times10^{-23}$ $m^3$ |
| $\eta_i$ , internal quantum efficiency | 0.8 |

**Table 2.** Extracted intrinsic parameters of the 1550 nm VCSEL

The frequency response of the VCSEL is represented in Figure 12, for different bias currents, including the simulated and experimental results. A good approximation is obtained between the simulated and experimental results.

## 4. OFDM and SC-FDMA over fiber applications

The VCSEL can be directly modulated using signals such as OFDM or SC-FDMA to encode digital data on multiple subcarrier frequencies. OFDM and SC-FDMA are used in applications such as wireless networks and LTE mobile communications. In order to avoid the high peak-to-average-power ratio (PAPR) inherent to OFDM modulation, the LTE standard employs SC-FDMA [16-18], an alternative modulation technique for the uplink with a similar low-complexity. Additionally, OFDM requires highly linear power amplifiers operating with a large backoff from their peak power, which results in low power efficiency [19]. In this context, it becomes pertinent to study the impact of employing SC-FDMA modulation within a RoF system based on directly modulated VCSELs.

### 4.1. Method and setup

The OFDM and SC-FDMA signal generation and demodulation is carried out in MATLAB environment. The experimental RoF setup illustrated in Figure 13 includes the Vector Signal Generator for the generation of the radio frequency (RF) signal that directly modulates the VCSEL, the optical fiber, the optical attenuator, and the optical receiver. The received signal is then sampled with a digital sampling oscilloscope at 20 Gsamples/s for offline demodulation in MATLAB. The validation of the transmitter and receiver blocks was performed in back-to-back configuration, by comparison with the theoretical PAPR results from the literature.

http://dx.doi.org/10.5772/61118

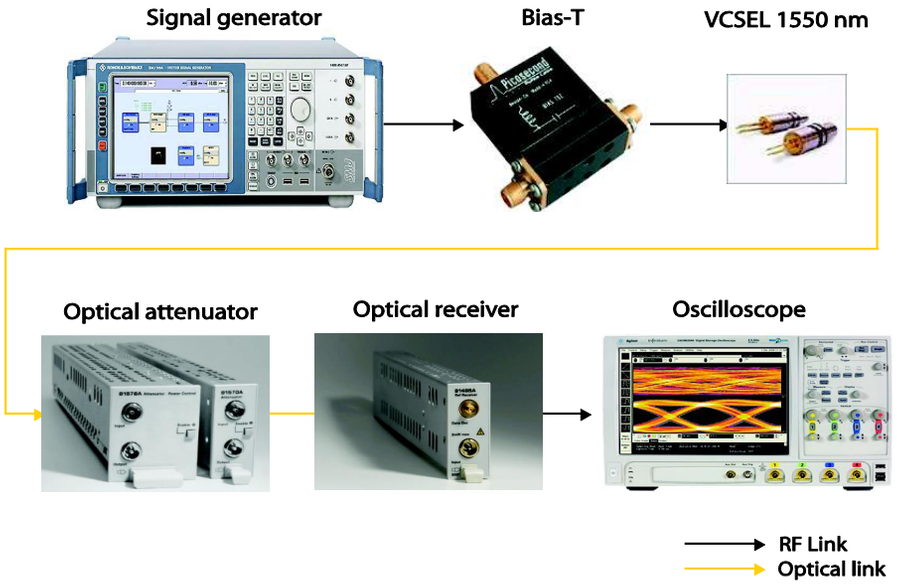


**Figure 13.** Experimental setup.

### 4.2. Transmitter

Both OFDM and SC-FDMA signals were modulated with a bit sequence, using three different possible modulation formats: QPSK (Quadrature Phase Shift Keying), 16-QAM (Quadrature Amplitude Modulation) and 64-QAM. Pilot subcarriers were added to the resulting symbols to estimate the effect of channel propagation. A diagram of both transmitters is shown in Figure 14.

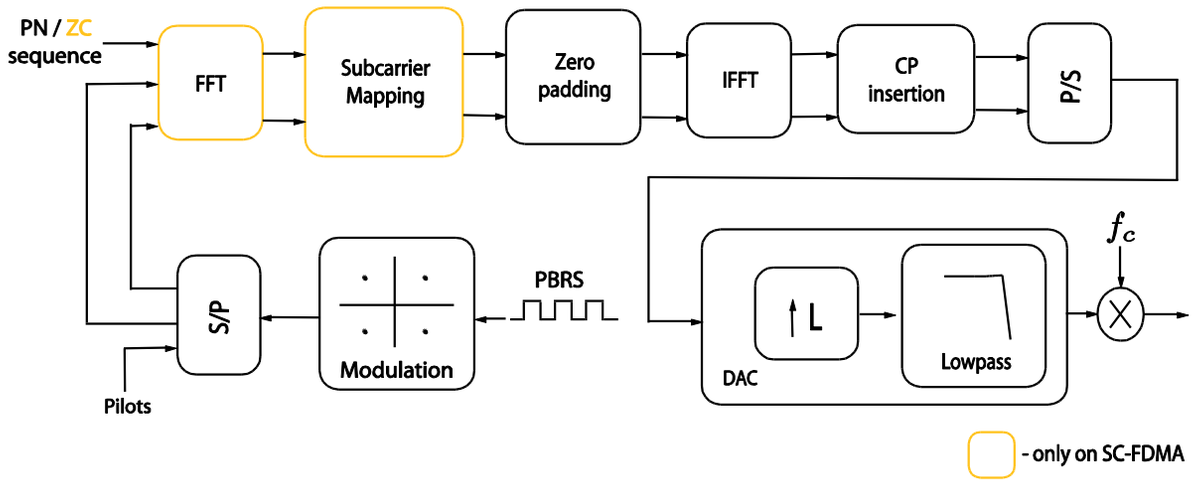


**Figure 14.** OFDM and SC-FDMA transmitters.

In the case of OFDM, the first symbol is used to facilitate time synchronization (finding the first symbol of the signal) at the receiver. This symbol is obtained using the inverse fast Fourier

transform (IFFT) of a sequence formed by the real part of a pseudorandom noise sequence at even frequencies and by zeros at odd frequencies, as proposed by Park [20]. After applying zero padding (adding zeros on both sides of the signal spectrum) in order to ease the filtering operation, a N-point IFFT is applied to convert the signal to the time domain. Before the digital-to-analog converter (DAC) where the signal is upsampled, the cyclic prefix (CP) (copy of the last part of the signal) is added to prevent multipath delay. Finally, the signal is upconverted to a RF carrier.

In the case of SC-FDMA, a Zadoff-Chu sequence [21] is used in the LTE standard, which functions as the first SC-FDMA symbol for synchronization purposes at the receiver. After this, a N-point fast Fourier transform (FFT) is performed and the resulting N subcarriers are mapped into M subcarriers using one of two different mapping methods: the interleaved mapping also known as interleaved frequency division multiple access, where the subcarriers are equidistantly distributed over the entire spectrum; and the localized mapping, also called localized frequency division multiple access, where the subcarriers are confined to a fraction of the spectrum. Thereafter, the zero padding and M-point IFFT are applied. Lastly, the CP is added and, as in the case of OFDM, the upsampling and the upconversion operations are performed.

In order to allow the performance comparison between the two modulation formats, only one user is considered.

The In-phase (*I*) and Quadrature (*Q*) components of both modulations formats were loaded to the signal generator, represented in Figure 13, where the frequency and the power of the RF-transmitted signal was specified.

### 4.3. Receiver

As shown in Figure 15, the received OFDM signal is first baseband filtered, to eliminate the noise outside the band, and then downconverted at the same frequency specified on the generator in order to obtain the baseband signal, followed by the lowpass filtering to remove the harmonics generated. Then the downsampling and quantization operations are applied to the signal followed by a temporal synchronization using Park's method. Then, the inverse of the operations carried out in the OFDM transmitter are performed at the receiver, namely the channel estimation and corresponding equalization in the frequency domain, followed by the removal of both the pilot subcarriers after the FFT and zero padding operations.

In the case of the SC-FDMA receiver, the operations are as follows: first baseband filtering, then temporal synchronization using the cross-correlation between the received signal and the reference signal (Zadoff-Chu sequence), and finally downconversion and downsampling. In order to recover the transmitted symbols, the inverse of the operations carried out at the SC-FDMA transmitter are performed at the receiver, including the channel estimation and the frequency domain equalization, similarly to the case of the OFDM receiver, after the IFFT and the subcarrier demapping.

http://dx.doi.org/10.5772/61118

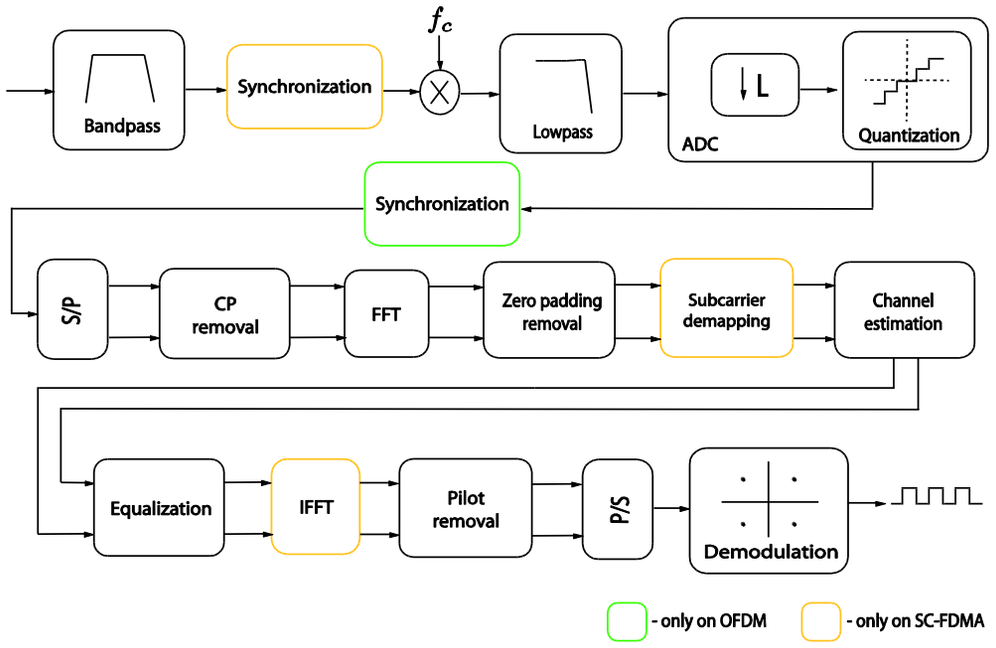


**Figure 15.** OFDM and SC-FDMA receivers.

## 5. System performance assessment

In this section, we present and discuss the relevant results using the signal-to-noise ratio (SNR) as a figure of merit to compare the OFDM and SC-FDMA signals with the same signal parameters.

### 5.1. Signals parameters

The signals generated are characterized by the following parameters: 16-QAM modulation, 10 Mbps, 1 user, 128 subcarriers, 8 pilot subcarriers for channel estimation, $4 \times \mathrm{FFT}_{size} = 512$ of zero padding, CP of $\mathrm{FFT}_{size}/4 = 32$, 11 transmitted symbols (1st symbol for synchronization and the others for data) and RF carrier located at 2.4 GHz. On the receiver side, the zero forcing equalization is used after the least squares channel estimation.

### 5.2. Analysis

We now assess the performance of a RoF system and compare the performance of OFDM and SC-FDMA wireless signals over fiber. Theoretically, the optical SNR is given by the following equation [22]:

$$\mathrm{SNR} = \frac{I_{RX}^2}{I_{RIN}^2 + I_{SN}^2 + I_{TH}^2 + I_{IMI}^2} \tag{29}$$

where the four noise currents are: $I_{RIN}^2$ is the RIN noise current, $I_{SN}^2$ is the shot noise current, $I_{TH}^2$ is the thermal noise current due to equivalent load resistance and pre-amplifier noise, and $I_{IMI}^2$ is the noise current due the intermodulation distortion. For lower modulation indices, the RIN is dominant in comparison to the thermal and the quantum noises [23].

The performance of the system is assessed on the basis of SNR or the error vector magnitude (EVM) figures of merit. The EVM expresses the quality of a digital modulated signal and is defined as the difference vector between the measured and the reference signals. Then the SNR can be calculated from the EVM. These figures of merit are calculated as follows:

$$\mathrm{EVM} = \frac{\frac{1}{N_S}\sum_{p=0}^{N_S}\left|S_{p,i} - S_{p,m}\right|^2}{\frac{1}{N_S}\sum_{p=0}^{N_S}\left|S_{p,i}\right|^2} \tag{30}$$

$$\mathrm{SNR} = \left(\frac{1}{\mathrm{EVM}}\right)^2 \tag{31}$$

where $S_i$ and $S_m$ are the ideal and measured constellations, respectively, $p$ is the constellation symbol index, and $N_S$ is the number of constellation symbols.

In Figures 16 to 18, the SNR results for OFDM and SC-FDMA transmissions are represented for three different laser bias currents ($I_0$= 4, 5, and 6 mA) as a function of the RF signal power, which is defined as:

$$P_{RF} = 10\log_{10}\left(\tau_{i,signal} Z_0\right) + 30\left[\mathrm{dBm}\right] \tag{32}$$

where $\tau_{i,signal}$ is the signal variance and $Z_0$ is equal to 50 Ω.

From the results presented, it is possible to conclude that there is a good matching between the simulation and the experimental results. It is clear from Figures 16 to 18 that for lower RF power, noise is dominant whereas for higher RF power, the intermodulation distortion, introduced by the VCSEL, becomes the limiting performance factor. The SC-FDMA signal is more sensitive to noise then the OFDM signal for lower RF power, while for higher RF power, the SC-FDMA signal is more robust to the intermodulation distortion. Despite this fact, the maximum SNR values attained are identical in both cases, albeit at a higher RF power for the SC-FDMA case, with no clear performance improvement of the SC-FDMA with respect to the OFDM.

http://dx.doi.org/10.5772/61118

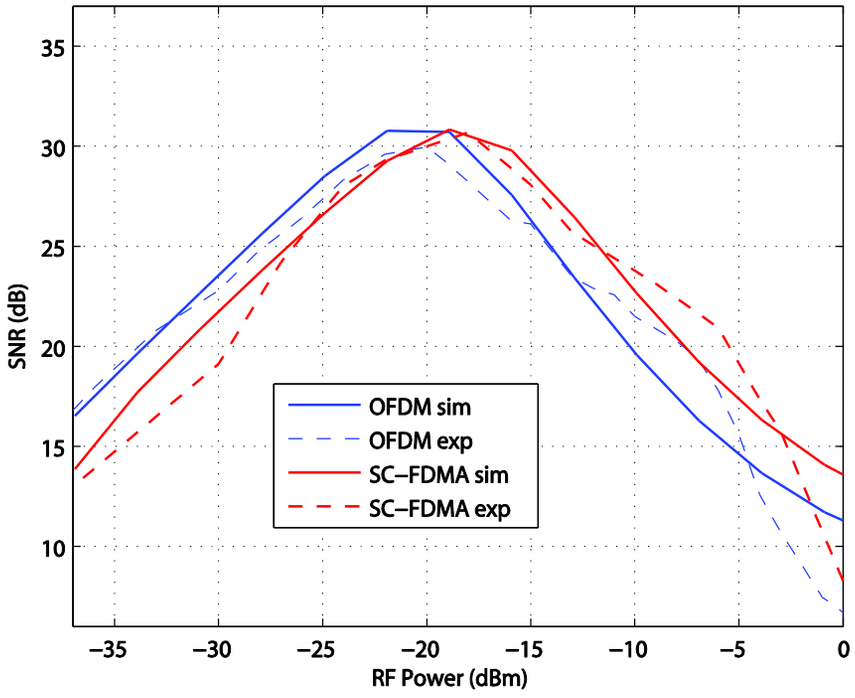


**Figure 16.** Simulated and experimental SNR for both OFDM and SC-FDMA as a function of the RF power for *Io* = 4mA.

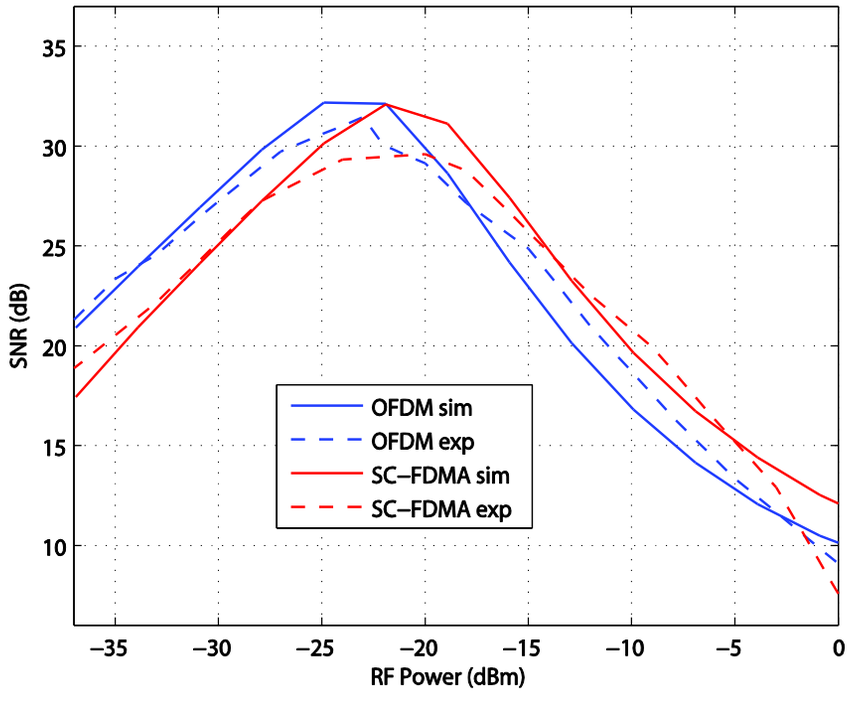


**Figure 17.** Simulated and experimental SNR for both OFDM and SC-FDMA as a function of the RF power for *Io* = 5mA.

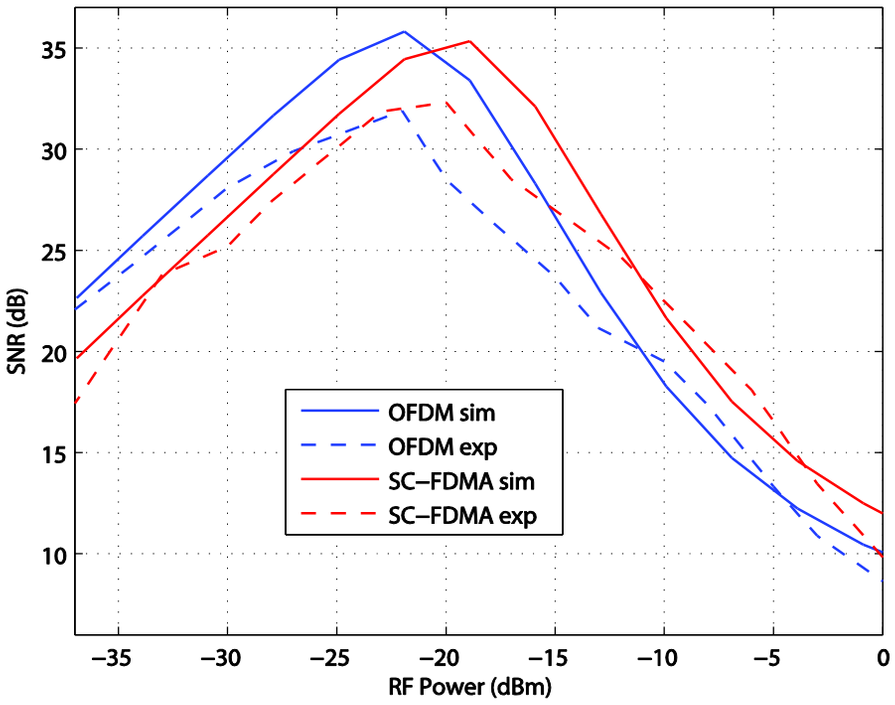


**Figure 18.** Simulated and experimental SNR for both OFDM and SC-FDMA as a function of the RF power for *Io* = 6mA.

## 6. Conclusion

We have assessed the performance of OFDM and SC-FDMA in the context of a RoF scenario, based on a directly modulated VCSEL operating at 1550 nm, and direct detection. To that purpose an accurate theoretical model of the laser was presented, for which device parameters were extracted based on fitting the model to experimental data of frequency response and input impedance. The simulation model fits well the experimental results, and we conclude that the SC-FDMA modulation presents a lower PAPR than the OFDM modulation as expected. Moreover, it is observed that the SC-FDMA is more susceptible to noise, yet it is more immune to intermodulation distortion than the OFDM modulation.

## Acknowledgements

We acknowledge support from Project "NORTE-07-0124-FEDER-000058" financed by the North Portugal Regional Operational Programme (ON.2 - *O Novo Norte*), under the National Strategic Reference Framework (NSRF), through the European Regional Development Fund (ERDF), and by national funds, through the Portuguese funding agency, *Fundação para a Ciência e a Tecnologia* (FCT). This work was carried out with the support of the TEC4SEA research infrastructure (www.tec4sea.com).

## Author details

Henrique M. Salgado[1,2*], Rúben E. Neto[2], Luís M. Pessoa[2] and Pedro J. Batista[1,2]

*Address all correspondence to: hsalgado@inesctec.pt

1 Faculdade de Engenharia da Universidade do Porto, Portugal

2 Instituto de Engenharia de Sistemas e Computadores – Tecnologia e Ciência - INESC TEC, Porto, Portugal

## References

[1] Chun-Ting Lin, Chen J, Peng-Chun Peng, et al. Hybrid optical access network integrating fiber-to-the-home and radio-over-fiber systems. IEEE Photonics Technology Letters. 2007;19(8):610-612.

[2] 3GPP. LTE [Internet]. Available from: http://www.3gpp.org/technologies/keywords-acronyms/98-lte [Accessed: January 6, 2014].

[3] Tauber D, Wang G, Geels RS, Bowers JE, Coldren LA. Large and small signal dynamics of vertical cavity surface emitting lasers. Applied Physics Letters. 1993;62(4):325

[4] Marcuse D. Classical derivation of the rate equation. IEEE Journal of Quantum Electron. 1983;19(8):1228-1231.

[5] Westcott J. Investigation of multiple f.m./f.d.m. carriers through a satellite t.w.t. operating near to saturation. Proceedings of the Institution of Electrical Engineers. 1967;114(6):726-740.

[6] Petermann K. Laser Diode Modulation and Noise. Advances in Opto-Electronics (ed.). Netherlands: Springer; 1988, p. 315. DOI: 10.1007/9789400929074

[7] Coldren LA, Corzine SW, Mashonavitch ML. Diode Lasers and Photonic Integrated Circuits (2nd ed.). John Wiley and Sons, Inc.; 2012, p. 744. DOI: 10.1002/9781118148167

[8] Bruensteiner M, Papen GC. Extraction of VCSEL rate-equation parameters for low-bias system simulation. IEEE Journal of Selected Topics in Quantum Electronics. 1999;5(3):487-494.

[9] Salgado H. Performance Assessment of Subcarrier Multiplexed Optical Systems: Implications of Laser Nonlinearities. Ph. D. dissertation. School of Electronic Engineering and Computer Systems, 1993.

[10] Tucker RS, Pope DJ. Microwave circuits models of semiconductor injection lasers. IEEE Transactions on Microwave Theory and Techniques. 1983;31(3):289-294

[11] Tucker RS, Kaminow IP. High-frequency characteristics of directly modulated InGaAsP ridge waveguide and buried heterostructures. Journal of Lightwave Technology. 1984;2(4):385-393.

[12] Agilent Technologies. De-embedding and embedding S-parameters networks using a vector network analyzer: Application Note 1364-1.2004.

[13] Agilent Technologies. In-fixture measurements using vector network analyzers: Application Note AN1287-9. 2006.

[14] Morton PA, Tanbun-Ek T, Logan RA, et al. Frequency response subtraction for simple measurement of intrinsic laser dynamic properties. IEEE Photonics Technology Letters. 1992;4(2):133-136.

[15] Silva S, Salgado HM. VCSEL Laser characterization and modelling for future optical transceiver at the super Large Hadron Collider. In: Transparent Optical Networks, 11th International Conference held on June 28, 2009--July 2, 2009. Azores: IEEE; 2009, p. 1-5.

[16] Ciochina C, Sari H. A review of OFDMA and single-carrier FDMA. In: Wireless Conference (EW), European held from 12-15 April 2010. Lucca: IEEE; 2010, p. 706-710.

[17] Myung HG. Introduction to single carrier FDMA. In: 15th European Signal Processing Conference held from 3-7 September 2007. Poznań, Poland: EURASIP, 2007.

[18] Myung HG, Junsung Lim, Goodman D. Peak-to-average power ratio of single carrier FDMA signals with pulse shaping. In: Personal, Indoor and Mobile Radio Communications, 2006 IEEE 17th International Symposium held from 11-14 September 2006. Helsinki: IEEE; 2006, p. 1-5.

[19] Myung HG, Junsung L, Goodman D. Single carrier FDMA for uplink wireless transmission. IEEE Vehicular Technology Magazine. 2007;1(3):30-38.

[20] Byungjoon Park, Cheon H, Kang C, Daesik Hong. Novel timing estimation method for OFDM systems. IEEE Communications Letters. 2003;7(5):239-241.

[21] Chu D. Polyphase codes with good periodic correlation properties. IEEE Transactions on Information Theory. 1972;18(4):531-532.

[22] Keiser G. Optical Fiber Communication (4th ed.). New York: McGraw-Hill Science/Engineering/Math; 2010, p. 688.

[23] Coelho D, Oliveira JMB, Pessoa LM, Salgado M, Castro JCS. Performance analysis of WDM-PON architecture for UWB distribution in aircraft networks. i-ETC:ISEL Academic Journal of Electronics, Telecommunications and Computers. 2013;2(1):ID16.